Bone Profiles: Simple, Fast, and Reliable Spine Localization in CT Scans

Jiří Hladůvka, David Major and Katja Bühler

Abstract Algorithms centered around spinal columns in CT data such as spinal canal detection, disk and vertebra localization and segmentation are known to be computationally intensive and memory demanding. The majority of these algorithms need initialization and try to reduce the search space to a minimum. In this work we introduce *bone profiles* as a simple means to compute a tight ROI containing the spine and seed points within the spinal canal. Bone profiles rely on the distribution of bone intensity values in axial slices. They are easy to understand, and parameters guiding the ROI and seed point detection are straight forward to derive. The method has been validated with two datasets containing 52 general and 242 spine-focused CT scans. Average runtimes of 1.5 and 0.4 s are reported on a single core. Due to its slice-wise nature, the method can be easily parallelized and fractions of the reported runtimes can be further achieved. Our memory requirements are upper bounded by a single CT slice.

1 Introduction

Image analysis methods focussing on spinal columns in CT scans such as detection, localization and segmentation of disks, vertebrae and spinal canal need high computational power and memory. This is particularly true for scans containing lower extremities or even full body scans. In such cases it turns out that for any spine related image processing task a significant portion of the CT data is unnecessary to deal with. Slices containing legs, which often make up the half of the data, can be left

---

J. Hladůvka (✉) · D. Major · K. Bühler
VRVis Center for Virtual Reality and Visualization, Donau-City-Strasse 1,
1220 Vienna, Austria
e-mail: jiri.hladuvka@vrvis.at

D. Major
e-mail: david.major@vrvis.at

K. Bühler
e-mail: katja.buehler@vrvis.at

J. Yao et al. (eds.), *Recent Advances in Computational Methods and Clinical Applications for Spine Imaging*, Lecture Notes in Computational Vision and Biomechanics 20, DOI 10.1007/978-3-319-14148-0_15

out already during volume reconstruction from the DICOM input. Parts too far from the spinal canal can be ignored during the search for vertebrae and intervertebral disks.

In this work we present a fast, memory efficient and easy to implement method to find bounding boxes around spinal columns and to propose reliable initialization seeds for subsequent algorithms. We propose a one-pass, slice-wise method based on simple bone distribution signatures. It is:

slice-wise, i.e. memory-efficient. Every DICOM slice is processed independently of the others. Memory requirements shrink to allocation of one image.

one-pass, i.e. fast. Each slice needs to be processed only once. The runtime therefore scales linearly with the total number of slices and the slice resolution. Being slice-wise the algorithm is furthermore suitable for parallelization, e.g. a map-reduce paradigm.

easy to implement. Contrary to machine learning approaches, we propose simple, threshold-based, bone-distribution descriptors and map-reduce them into 1D arrays referred to as *bone profiles*. The algorithm has 6 easy to understand parameters. We list them together with the values used for the validation.

The rest of this paper is organized as follows: We briefly describe state-of-the-art in Sect. 2. In Sect. 3 we propose simple bone distribution descriptors and introduce their aggregation in bone profiles. In Sect. 4 we show how the profiles help localizing the spine. The proposed method is evaluated in Sect. 5. This paper ends with discussion and conclusions in Sect. 6.

2 Related Work

Spine ROI localization is conducted as an initial step in the literature in order to accelerate the detection and segmentation of the spinal parts. The authors of [3] start with a slice-wise detection of candidate positions located on bones and extend the positions to regions where features are extracted. The features are then compared to a sample set of previously annotated vertebra regions to find the best candidate which surrounds the vertebra. The approach of [7] extracts disk clue points and fits polynomials to them on every sagittal slice of an MR scan. Vertebra height statistics are computed along the fitted polynomials and the polynomial with the minimum vertebra height variance indicates the slice for further processing. Stern et al. [8] work with 3D CT and MR scans. They extract the spinal centerline by using gradient vectors of opposite pairs of vertebral body edge points. In [10] at first spine regions are localized slice-wise through thresholding and connected component analysis. The watershed algorithm is then used to extract spinal canal candidates. Graph search helps to find the spinal canal. Klinder et al. [5] apply Generalized Hough Transform using vertebral foramen meshes. The global maximum in the Hough space corresponds to a position in the spinal cord. Kelm et al. [4] localize spine regions roughly as a first step such as we do. However, they apply the Marginal Space Learning algorithm on machine learned position candidates in CT and MR scans. In summary and in contrast to our work, the aforementioned algorithms for spine localization use either more costly features, or more complex machine-learned models, or a combination of both.

3 Bone Distribution Descriptors and Profiles

We assume sequences of axial CT slices with known z coordinate and pixel spacing, both given in millimeters. We denote the pixel positions in the patient coordinates as $\mathbf{p} = (p^x, p^y, p^z)$. For sake of simplicity we also assume the feet-to-head, face-up (supine) orientation of the patient. The pixel gray values will be denoted as $g = g(\mathbf{p})$ and we assume them to be in Hounsfield units.

Our approach is based on bone distribution signatures within slices. For a fixed slice at location z we are therefore first interested in a *rough* segmentation $\mathscr{B}_z$ of the bones. Given the Hounsfield intensities g, this can be achieved by an interval threshold, i.e., using two constants:

$$\mathscr{B}_z = \{\mathbf{p} = (p^x, p^y, p^z) \;\mid\; p^z = z \,\wedge\, g(\mathbf{p}) \in [400, 1050]\} \tag{1}$$

3.1 Centroids and Deviations

The simplest features are based on the centroid of segmentations $\mathscr{B}_z$

$$\boldsymbol{\mu}_\mathbf{z} = \frac{1}{|\mathscr{B}_z|} \sum_{\mathbf{p} \in \mathscr{B}_z} \mathbf{p} = (\mu_z^x, \mu_z^y, z) \tag{2}$$

and on the length σ_z of the associated standard deviation vector

$$\sigma_z = \sqrt{\frac{1}{|\mathscr{B}_z| - 1} \sum_{\mathbf{p} \in \mathscr{B}_z} (p^x - \mu_z^x)^2 + (p^y - \mu_z^y)^2}. \tag{3}$$

Centroids $\boldsymbol{\mu}_\mathbf{z}$ correlate with the spine reliably in the lumbar slices where pelvis, ribs, or head do not contribute to it.

The lumbar part can be characterized by deviation lengths σ_z related to size of a vertebra seen in an axial slice [9]. Values of σ_z larger than 40 mm indicate presence of non-vertebra bones.

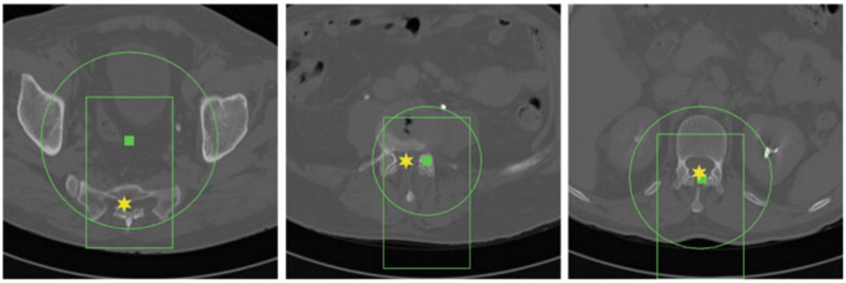

Fig. 1 Examples showing centroids $\boldsymbol{\mu}_\mathbf{z}$ (*square*), a *circle* of radius σ_z, the 80 × 140 mm refinement window (*rectangle*), and refined center $\boldsymbol{\nu}_\mathbf{z}$ (*star*)

Centroid refinement. While reliable in the lumbar area, the centroids $\boldsymbol{\mu}_\mathbf{z}$ may drift remarkably from the spine if the pelvis or ribs contribute by their pixels (cf. Fig. 1).

To avoid this we refine the centroids $\boldsymbol{\mu}_\mathbf{z}$ within rectangular 80 × 140 mm windows, asymmetrically spanned around them:

$$\mathscr{W}_z = \{\mathbf{p} \in \mathscr{B}_z \mid -40 \leq p^x - \mu_z^x \leq 40 \ \wedge \ -40 \leq p^y - \mu_z^y \leq 100\} \tag{4}$$

The size of the windows is set to be sufficiently big to accommodate any vertebra in an axial view [9] and to account for relative positions of the centroids and vertebrae in pelvis slices. The centroids $\boldsymbol{\mu}_\mathbf{z}$ are refined to the center $\boldsymbol{\nu}_\mathbf{z}$ of bone pixels in this window:

$$\boldsymbol{\nu}_\mathbf{z} = \frac{1}{|\mathscr{W}_z|} \sum_{\mathbf{p} \in \mathscr{W}_z} \mathbf{p} \tag{5}$$

3.2 Shape Histograms: AP Versus LR Distribution

To identify leg slices, we propose to discriminate slices with bone distributions dominant in the left-to-right direction and zero contributions in the anterior-posterior direction (see Fig. 2).

We construct 4-bin histograms located in the refined centers $\boldsymbol{\nu}_\mathbf{z}$. Putting $\delta = \mathbf{p} - \boldsymbol{\nu}_\mathbf{z}$ we define the following four quantities:

$$h_z^A = |\{\mathbf{p} \in \mathscr{B}_z \mid \delta^y < -|\delta^x| \leq 0\}| \tag{6}$$

$$h_z^P = |\{\mathbf{p} \in \mathscr{B}_z \mid \delta^y > \ \ |\delta^x| \geq 0\}| \tag{7}$$

$$h_z^R = |\{\mathbf{p} \in \mathscr{B}_z \mid \delta^x < -|\delta^y| < 0\}| \tag{8}$$

$$h_z^L = |\{\mathbf{p} \in \mathscr{B}_z \mid \delta^x > \ \ |\delta^y| > 0\}| \tag{9}$$

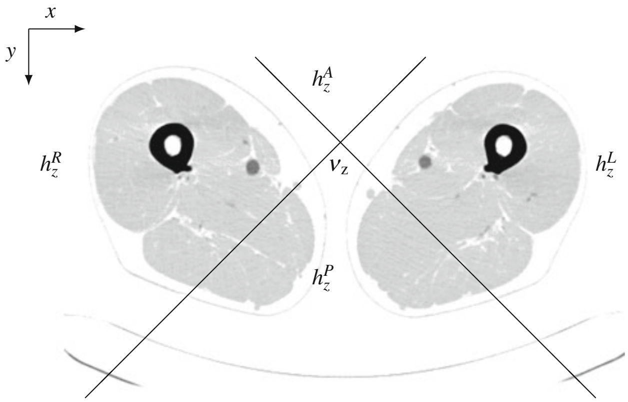

Fig. 2 *Right*, *left*, ante, and poste histogram bins centered at $\boldsymbol{\nu}_z$ overlaid over a negative of a CT slice at position z showing legs and table

With the AP/LR histograms we reformulate the leg detection as a search for slices, where ante-poste bone contributions vanish. We introduce scalars λ_z and a threshold to yield this:

$$0 \leq \lambda_z = \frac{h_z^A}{h_z^L + h_z^R} < 0.04 \tag{10}$$

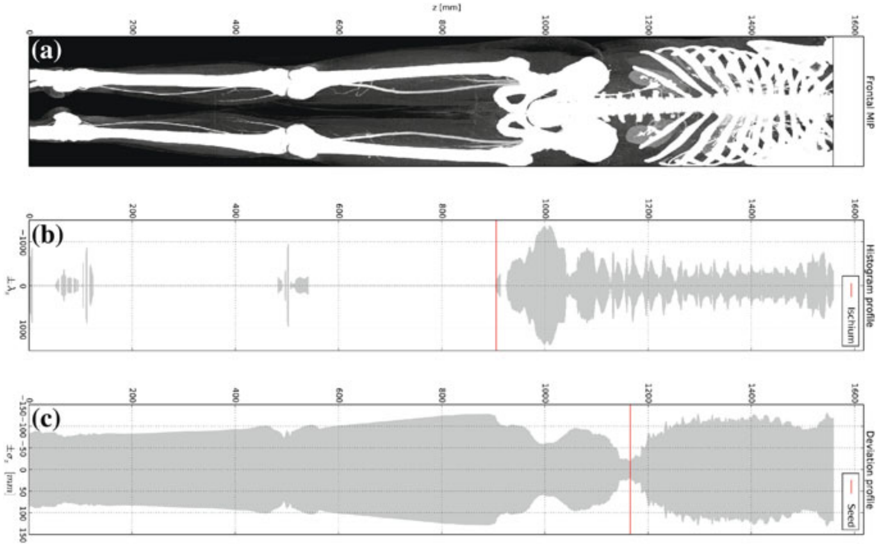

Fig. 3 An example CT scan in a frontal maximum intensity projection (MIP) (**a**), its histogram profile (**b**) and deviation profile (**c**)

Note that we exclude the posterior voxels h_z^P from (10) in order to ignore eventual contribution of a CT table.

3.3 Bone Profiles

In the previous section we have introduced two bone distribution descriptors, i.e. scalars λ_z and σ_z for every slice z. Next we aggregate them into two 1D arrays indexed by z and refer to as the *bone profiles*. A symmetric plot of bone profiles along the z-axis is shown in Fig. 3.

4 Applications to Spinal Column Localization

In this section we show how the bone profiles and the refined centers $\boldsymbol{v}_\mathbf{z}$ can be used to bound the spinal column and to identify a reliable initialization seed for subsequent computations.

4.1 Discarding the Slices up to the Ischium

When dealing with spines, leg slices should be taken out of consideration. We observed that the first occurrence of vanishing λ_z in the top-to-bottom order may correspond either to the bottom of sacrum or the bottom of the pelvis—the ischium (cf. Fig. 3b).

In order to have a security margin between the spine and the slices to drop we suggest to identify *ischium* slices. We identify them by the first 65 mm long segment of zeros in the histogram profile, i.e. a sequence longer than the average distance from ischium to bottom of sacrum.

4.2 Seeding a Spinal Canal Search

Algorithms using incremental/propagated search need to be initialized [5]. To obtain a reliable seed point near the spinal canal we consider the refined center $\boldsymbol{v}_{\mathbf{z}^\star}$ in a slice with minimal deviation σ_z (cf. Eq. 11). In this case no other bones except for vertebra contribute to the signatures and the point $\boldsymbol{v}_{\mathbf{z}^\star}$ yields an estimate of the spinal canal. Such slices are predominantly found either in the lumbar area between pelvis and the first rib (cf. Fig. 3c) or in the neck area.

$$\boldsymbol{v}_{\mathbf{z}^\star} \quad | \quad z^\star = \operatorname{argmin}\{\sigma_z\} \tag{11}$$

4.3 Bounding the Spinal Column

Machine learning methods need to compute a vector of features at every voxel. Reducing the amount of voxels to be classified to a minimum can therefore significantly speed up such algorithms. After the leg slices have been discarded we wish to further prune the space by setting coronal and sagittal bounding planes.

For healthy spines the previously found seed $\boldsymbol{v}_{\mathbf{z}^\star}$ could be reused to set up a bounding box of a predefined size. Such an approach would, however, fail for scolioses and other spine curvature related disorders.

To deal with such cases we derive coronal and sagittal planes from the bounding box of the 80 × 140 mm windows (cf. Eq. 4) spanned symmetrically around a *subset* of centers $\boldsymbol{v}_{\mathbf{z}}$. The refined centers $\boldsymbol{v}_{\mathbf{z}}$ are first sorted by a *drift reliability* $\Delta_z = ||\boldsymbol{v}_{\mathbf{z}} - \boldsymbol{\mu}_{\mathbf{z}}||$ from the original centroids $\boldsymbol{\mu}_{\mathbf{z}}$: the smaller the drift the more reliable the center. A fraction of sorted $\boldsymbol{v}_{\mathbf{z}}$ involved in spanning bounding planes balances the tightness of bounding around spinal column and the data reduction. It is the last and the only free parameter in our method.

5 Results

Data and timing. All experiments were performed on two datasets. Dataset 1 contained 52 diversely cropped CT scans from three different vendors including 18 instances with legs up to abdomen and 34 scans with torso and/or head with neck. 29 out of the 52 were CTA scans containing contrast-enhanced vessels. The pixel sizes of the 512 × 512 axial images range from 0.26 to 1 mm, and the slice distances vary from 0.1 to 3 mm. The smallest and largest scan comprised of 103 and 5,966 slices respectively. Ground truth (ischium slice, spinal canal centers and vertebral body centers) was generated by a medical expert. For Dataset 2 we used the annotated spine CT database for benchmarking of vertebrae localization and identification with 242 spine-focused CT scans containing varying pathologies [2] (publicly available at http://spineweb.digitalimaginggroup.ca). Vertebral body centers were present for this dataset, ischium and spinal canal centers were added. The time performance has been measured single threaded on an Intel Core i7 2.6 GHz machine. The computation of both profiles took on average 1.5 s for Dataset 1 and 0.4 s for Dataset 2.
Discarding the leg slices. The ischium identification quality was measured in the 18 CT scans of Dataset 1 where legs were present. The mean error from the true ischium slice was 16.5 ± 13.2 mm which yields a sufficiently tall margin to the bottom of the spine, i.e. no cropping of the spine was observed. The amount of voxels has been reduced by a factor of 2.5 on average. For the remaining 276 scans without leg slices we counted the false positive occurrence of an ischium slice which was 0.
Seed detection. To assess the quality of the seeds $\boldsymbol{v}_{\mathbf{z}^\star}$ we evaluated their distribution w.r.t. the associated spinal canal centers (cf. Fig. 4). Table 1 summarizes the seed detection results: the average x- and y-deviations of $\boldsymbol{v}_{\mathbf{z}^\star}$ from spinal canal centers

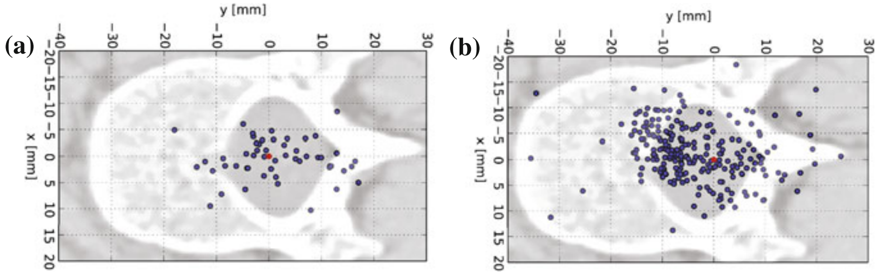

Fig. 4 Distribution of seeds vz for all instances of Dataset 1 (**a**) and Dataset 2 (**b**) relative to the ground truth spinal canal centers (located at origin) overlaid on an example slice (Color figure online)

Table 1 x- and y-deviations of detected spinal canal seeds from ground truth annotations and spinal canal identification rate (CIDR) for Dataset 1 and 2

	x-deviation (mm)	y-deviation (mm)	CIDR (%)
Dataset 1	2.8 ± 2.4	6.8 ± 5.0	75
Dataset 2	4.0 ± 3.3	8.0 ± 5.6	79

and the spinal canal identification rates (CIDR) for both datasets. The spinal canal identification rate indicates how often the seeds hit the spinal canal. For data where the seed was not detected within the spinal canal (25 % in Dataset 1 and 21 % in Dataset 2), it was placed either on the vertebral arch or on the vertebra body.

Bounding the spinal column. In order to evaluate the accuracy and utility of the spinal column bounding we analyzed how well spine ground truth was covered by the planes and to what amount data was reduced. As for the spine coverage, all expert-annotated vertebral body centers were contained within the coronal and sagittal bounding planes. To see the accuracy of the spine coverage of whole vertebrae we measured the minimum distances between the vertebral body center annotations and the left/right sagittal planes (Δx), the anterior coronal plane (Δy^A) and the posterior coronal plane (Δy^P) for each scan. Two distinct distances in the y-direction were necessary because of the sagittal asymmetry of vertebrae around the vertebral body center. In order to see if our bounding planes crop into vertebrae, we compared Δx to the half of the average midtransverse diameter ($l_x = 22.5\,\text{mm}$) of lumbar vertebrae [9], Δy^A to the half of the average inferior width of lumbar vertebral bodies ($l_y^A = 17\,\text{mm}$) and Δy^P to the average sagittal distance from vertebral body center to spinous process ($l_y^P = 65\,\text{mm}$) of lumbar vertebrae [1]. As higher percentages of reliable seeds stretched the bounding planes away from body centers (Sect. 4.3 and Fig. 6b), we investigated two percentage values, 40 and 90 %. For Dataset 1, 3 %(0 %) of the cases had slightly smaller Δx than l_x when using 40 %(90 %) of the most reliable seeds for bounding plane computation. l_x was not completely covered by 1.5 %(1 %) of the scans in Dataset 2 with 40 %(90 %) of the reliable seeds. These outliers were due to scoliosis in both datasets. Examples are shown in Fig. 5a, b.

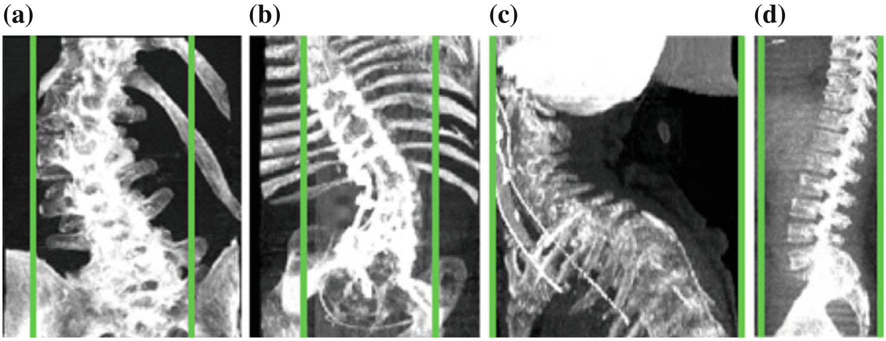

Fig. 5 MIPs of example data with bounding planes (*green lines*) generated by 40 % of the most reliable seeds. **a, b** Frontal MIPs of highly scoliotic spines. **c, d** Sagittal MIPs of cases where the input volume is cropped either on the anterior or on the posterior side near to vertebral body center annotations (Color figure online)

As for the Δy^A values, all of the cases had larger Δy^A values than l_y^A for both reliability percentages in Dataset 1. 1.6 % of the cases had smaller Δy^A values than l_y^A for both percentages in Dataset 2. These cases, however, were already too tightly cropped scans where expert annotations of vertebra centers were too close to the anterior volume border (see Fig. 5c) and our bounding planes did not further crop into the volume. The Δy^P values were in 5 % of the cases smaller than l_y^P for both reliability percentages in Dataset 1 which was due to tightly cropped input scans in the posterior direction with annotations close to the volume border (see Fig. 5d). In Dataset 2, 27 %(18 %) of the scans had smaller Δy^P values than l_y^P for 40 %(90 %) of the most reliable seeds. 4 CT scans out of the 27 % were slightly cropped. The remaining scans out of the 27 % and all cases out of the 18 % were handled correctly (full vertebra coverage) and either had annotations close to volume borders or contained vertebrae with smaller sagittal vertebral lengths than those of lumbar vertebrae (l_y^P).

To assess the utility of the spinal bounding planes, the average data reduction factor (DRF) was measured for both datasets after discarding the leg slices. It was 4.5(3.3) on average for Dataset 1 and 1.7(1.5) for Dataset 2 when considering 40 %(90 %) of the most reliable seeds for bounding plane construction.

6 Discussion and Conclusion

To the best of our knowledge, this is the first time a machine-learning-free method yields fast and reliable spine localization in such large (52 + 242) and diverse population of both normal and abnormal CT scans. Other machine-learning free related works (such as [3, 5]) achieve results with comparable accuracy to ours but they are slower and tested on much less data. Graf et al. [3] tested on 34 CT scans within an average time of approximately 1 minute per scan and Klinder et al. [5] needs 7.6 s to find an initial spine seed in a collection of 64 CT scans.

Machine-learning-based approaches [2, 4] are not only competitive enough based on accuracy to the method we proposed, but they were tested with similarly high amounts of data and achieved good time performances. Glocker et al. [2] used 242 spine CT scans (our Dataset 2) for testing and Kelm et al. [4] needed only 11.5 s on average for intervertebral disk detection and labeling. In the following we therefore discuss our work from the perspective of machine learning methods.

First, setting-up a machine learning method requires ground truth annotations which is a labor intensive and error-prone task.

Second, the state-of-the-art machine learning algorithms (i.e., decision trees, random forests) combine image features in unintuitive and hard to interpret ways [6]. Potential algorithm failures are consequently impossible to explain and fix. On the contrary we proposed six parameters with a clear interpretation and justification (see Table 2): two Hounsfield unit thresholds for rough bone segmentation (Eq. 1), width and height of the refinement and spanning rectangles (Eq. 4, Sect. 4.3) deduced from morphometry of vertebrae and pelvis. The threshold to distinguish between legs and the rest of the slices λ_z (Eq. 10) was set empirically and validated after plurality of ground annotations was available (see Fig. 6a). The amount of reliable seeds involved in bounding the spine (Sect. 4.3) yields a parameter to control the bounding tightness (see Fig. 6b). Increasing this amount increases the overall minimal distance of the planes to the vertebral body center annotations, i.e. it decreases the DRF (see Sect. 5). This is the only free parameter of our method and users may tailor it to own applications: 10 % assures bounding of all vertebral body centers, 40 % bounds whole vertebrae but some cases may get slightly cropped, 90 % contains only a small set of vertebrae not covered completely and 100 % guaranties full coverage of the spinal column.

The six parameters make our method easy to implement. In contrast, parameters inherent to machine learning based methods (e.g., tree depth, number of trees) need to be found in a cross-validation scheme [6]. Such parameter setups pose difficulties for researchers who desire to re-implement the algorithms for own purposes.

Finally, learning methods need to compute high dimensional feature vectors at every voxel to yield a class or a regression value *after* the volume has been

Table 2 Summary of parameters and their values used within this work

Parameter name	Parameter value
Bone segmentation threshold, low	400 HU
Bone segmentation threshold, high	1050 HU
Spanning rectangle, width	80 mm
Spanning rectangle, height	140 mm
Ischium detection threshold	0.04
Amount of most reliable seeds	10 %,40 %, 90 %,100 %

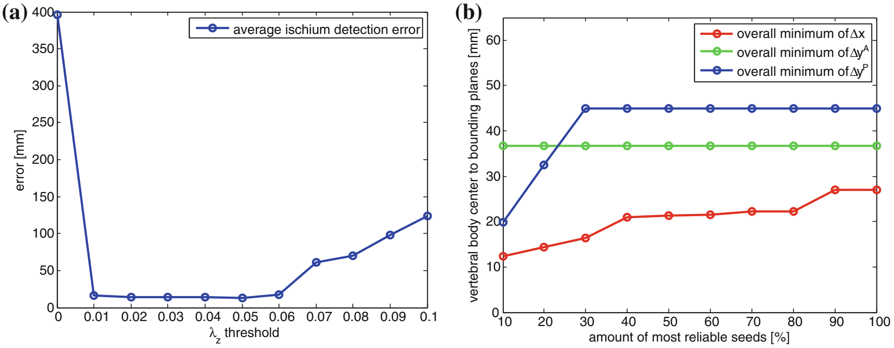

Fig. 6 **a** Empirical selection of parameter values for λ_z based on average ischium detection errors of Dataset 1. λ_z yields the least average error at 0.04. **b** Empirical parameter selection for the tightness of bounding planes based on Dataset 1. The values are minima of the 52 minimal distances ($\varDelta x$, $\varDelta y^A$ and $\varDelta y^P$).

reconstructed from the slices and loaded into memory. Moreover, data structures often involved in feature extraction (e.g., pyramids or integral volumes) demand additional memory. From perspective of machine learning methods, we thus introduced a computationally inexpensive tool to prune the search space. It is not clear how machine learning methods would perform with really big data. While the biggest of the currently available volumes of Dataset 2 is 256 MB, we were able to process a 3 GB scan in Dataset 1 within a memory required by one axial slice. We agree that the memory issue is irrelevant during research. It may, however, become a crucial argument for radiological departments who often pose tight memory constraints.

We have shown that our method delivers reliable results for spine localization within average times of 1.5 and 0.4 s for two sets of CT scans. It is faster compared to other methods such as [3] taking 1 min and [5] taking 7.6 s.

Possible weakness of our algorithm is related to the influence of artificial materials and artifacts with Hounsfield values similar to bones (e.g., contrast agents, implants, imaging artifacts). However, our results on CTA scans, pathological cases and scans from multiple vendors showed that our method is able to handle data with abnormalities and different imaging parameter settings correctly. A detailed study on this topic is left to future work.

Acknowledgments The competence center VRVis with the grant number 843272 is funded by BMVIT, BMWFW, and ZIT—The Technology Agency of the City of Vienna within the scope of COMET—Competence Centers for Excellent Technologies. The program COMET is managed by FFG. Thanks go to our project partner AGFA Healthcare for providing data and valuable input.

References

1. Gilad, I., Nissan, M.: Sagittal evaluation of elemental geometrical dimensions of human vertebrae. J. Anat. **143**, 115–120 (1985)
2. Glocker, B., Zikic, D., Konukoglu, E., Haynor, D.R., Criminisi, A.: Vertebrae localization in pathological spine CT via dense classification from sparse annotations. In: Medical Image Computing and Computer-Assisted Intervention, pp. 262–270. Springer, Berlin (2013)
3. Graf, F., Kriegel, H.P., Schubert, M., Strukelj, M., Cavallaro, A.: Fully automatic detection of the vertebrae in 2D CT images. In: SPIE Medical Imaging, Vol. 7962 (2011)
4. Kelm, B.M., Wels, M., Zhou, S.K., Seifert, S., Suehling, M., Zheng, Y., Comaniciu, D.: Spine detection in CT and MR using iterated marginal space learning. Med. Image Anal. **17**(8), 1283–1292 (2013)
5. Klinder, T., Ostermann, J., Ehm, M., Franz, A., Kneser, R., Lorenz, C.: Automated model-based vertebra detection, identification, and segmentation in CT images. Med. Image Anal. **13**(3), 471–482 (2009)
6. Kotsiantis, S.: Supervised machine learning: A review of classification techniques. Informatica **31**, 249–268 (2007)
7. Peng, Z., Zhong, J., Wee, W., Lee, J.h.: Automated vertebra detection and segmentation from the whole spine MR images. In: 27th Annual International Conference of the Engineering in Medicine and Biology Society, pp. 2527–2530 (2005)
8. Štern, D., Likar, B., Pernuš, F., Vrtovec, T.: Automated detection of spinal centrelines, vertebral bodies and intervertebral discs in CT and MR images of lumbar spine. Phys. Med. Biol. **55**(1), 247–264 (2010)
9. Van Schaik, J., Verbiest, H., Van Schaik, F.: Morphometry of lower lumbar vertebrae as seen on CT scans: newly recognized characteristics. Am. J. Roentgenol. **145**(2), 327–335 (1985)
10. Yao, J., O'Connor, S.D., Summers, R.M.: Automated spinal column extraction and partitioning. In: 3rd IEEE International Symposium on Biomedical Imaging: Nano to Macro, pp. 390–393 (2006)